ACTA PHYSICA POLONICA A No. 4 Vol. **147** (2025)

Studies of the Physical Properties of Sputter-Deposited ZnO, ZnO/Pt and ZnO/Pd Semiconductor Thin Films for Sensor Application

P. Struk[a,*], M.A. Borysiewicz[b] and M. Guziewicz[b]

[a] *Department of Optoelectronics, Faculty of Electrical Engineering, Silesian University of Technology, Gliwice, Poland*
[b] *Łukasiewicz Research Network — Institute of Microelectronics and Photonics, Warsaw, Poland*

Received: 13.08.2024 & Accepted: 24.02.2025

Doi: 10.12693/APhysPolA.147.298

*e-mail: przemyslaw.struk@polsl.pl

An investigation into the physical properties of the wide band gap oxide semiconductor material zinc oxide for sensors has been conducted. The investigation presented in this paper is divided into two sections. The first section focuses on the development of the deposition technology, investigation of physical properties (such as surface topography, crystalline structure, spectral transmission in the ultraviolet–visible–near infrared range, and the chemical composition) of the ZnO, ZnO/Pt, or ZnO/Pd layer. The other section focuses on the sensor's properties (changes in spectral transmission) of ZnO layers as a function of temperature or a selected gas environment (hydrogen). These investigations were carried out on the following structures: pure ZnO layer with a relatively low roughness surface, pure and porous ZnO layer, and porous ZnO layer doped with palladium or platinum. The results are a basis for the development of optoelectronic sensors, which serve the purpose of detecting hydrogen or temperature measurements.

topics: ZnO/Pt and ZnO/Pd physical properties, ZnO sensitivity properties, ZnO temperature sensor in ultraviolet-visible (UV-VIS), ZnO gas sensor

1. Introduction

The development of modern civilization is directly related to the development of industries such as the electronics industry, automotive industry, and chemical industry, as well as to the development of diagnosis methods in healthcare. In industry, temperature and gas environment control plays an important role. One of the most important gases used in industry is hydrogen. Hydrogen is necessary for a proper course of technological processes, for example, hydrotreating of petroleum products, chemical synthesis, and production of electrical energy by hydrogen cells [1–7]. It should be noted that hydrogen is dangerous and explosive in concentrations above the lower explosion limit of 4 mol% [8]. From that point of view, monitoring the hydrogen level is a key safety issue. Accordingly, it is important to develop semiconductor sensors, which can then be used to detect hydrogen concentration in the gaseous environment and temperature monitoring.

The core advantage of optoelectronic gas sensors, which operate based on changes in optical properties (spectral transmission) of the active layer (ZnO), is the high safety of gas detection. The measurement of optical properties of the active layer in a sensor eliminates the risk of explosion initialized by an electrical spark compared to electronic sensors based on resistance measurement. The most important issue concerning the development of gas or temperature sensors is the choice of a proper measurement method and a suitable material, which acts as the sensitive part of the sensor structure. An interesting group of materials that can be applied as an active layer in gas or temperature sensors are wide band gap oxide semiconductors. In this group, special attention is focused on zinc oxide semiconductors and their application in gas sensor structures, because they are sensitive and selective to gaseous environments, among others, hydrogen H_2 [7, 9–13]. The ZnO is a semiconductor material with a wide energy gap of $E_r \simeq 3.2$ eV and a light absorption edge of $\alpha_t \simeq 380$ nm and above, moreover, it is transparent to light [7, 10–15]. Additional advantages of ZnO semiconductors are their non-toxic properties and biocompatibility with human tissues [16–18].

The key issue in the application of the ZnO semiconductor in sensor structures is knowledge about its physical properties as a function of deposition technology and doping elements. The physical properties of ZnO semiconductor materials depend on the manufacturing technology and doping with materials such as Pt or Pd. In addition, doping ZnO with Pt or Pd significantly improves the properties of gas sensors dedicated to selected gas environments [17, 18].

Another issue is knowledge about the change of physical properties (ZnO) as a function of external conditions, such as gaseous environments and temperature.

This manuscript describes an investigation into the physical properties of ZnO nanostructures obtained by means of reactive magnetron sputtering in the form of a layer characterized by its low surface roughness (smooth layers) and porous structure, and additionally doped by either platinum (ZnO/Pt) or palladium (ZnO/Pd). The presented research focuses on the surface topography of the layers and their morphological structure, crystalline structure, chemical composition, spectral transmission in the ultraviolet–visible–near infrared (UV-VIS-NIR) regions, and the sensitivity of their optical properties as a function of the temperature or selected gaseous environment consisting of H_2 in a synthetic air mixture.

2. Sample fabrication

The investigated ZnO layers were divided into three groups: smooth surface (root mean square roughness R_q of a few nm), porous ZnO layer, and porous ZnO layer doped with either palladium or platinum. The selected ZnO/Pd and ZnO/Pt layers were also additionally annealed in order to diffuse the Pd or Pt layer deep into ZnO. The pure ZnO layers were deposited by a reactive magnetron sputtering on quartz substrates. The ZnO layers with a relatively small roughness ($\sim$ a few nm) were deposited with the use of radio-frequency (RF) mode from a 99.99% purity ZnO ceramic target in an atmosphere that was a mixture of oxygen O_2 (70%) and argon Ar (30%), at a total pressure of $P_{\mathrm{Ar+O}} = 7.8$ mTorr and a partial oxygen pressure of $P_{\mathrm{O}} = 2.5$ mTorr for a cathode current equal to $I_c = 0.14$ A. The porous ZnO, ZnO/Pt, and ZnO/Pd layers (thickness 400 nm) were prepared as follows: first, a 75 mm diameter, 4N-pure Zn target was sputtered in a Surrey NanoSystems γ-1000C reactor under 80 W DC power in a mixed argon–oxygen atmosphere. The argon flow was set to 10 sccm, the oxygen flow to 1 sccm, and the total pressure was kept at 3 mTorr. The gases used were 6N-pure. After deposition, the Zn underwent oxidation in a Mattson SHS 100 rapid thermal processing (RTP) furnace. The process took place in an oxygen flow at 600°C for 20 min, in accordance with our previous studies [19]. Pt or Pd were introduced in the form of 5 nm thin films either before the oxidation (porous ZnO/$\mathrm{Pt_{DBO}}$, ZnO/$\mathrm{Pd_{DBO}}$) in a part of the samples or after oxidation (porous ZnO/$\mathrm{Pt_{DAO}}$, ZnO/$\mathrm{Pd_{DAO}}$) in another part of the samples. The metals were deposited in a Leybold Z400 system using 4N-pure, 75 mm diameter targets under 50 W DC power. The working atmosphere was pure argon, kept under the pressure of 6 mTorr. The schematic view of the types of the investigated ZnO layers is presented in Fig. 1.

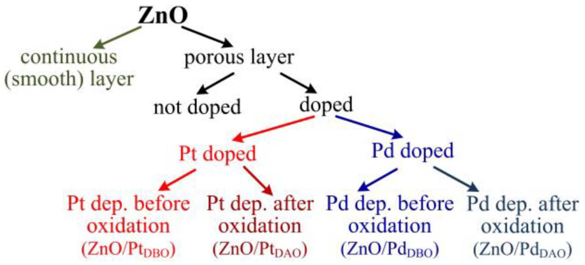

Fig. 1. Types of investigated ZnO thin films.

Palladium or platinum as dopant materials for ZnO layers were chosen due to their catalytic properties, which are especially desirable for the detection of hydrogen. The Pd and Pt catalytic materials allow us to dissociate molecular hydrogen into atomic hydrogen, which is highly reactive in contact with the semiconductor surface.

3. Experimental setup and methods

The initial research stage focused on the investigation of the surface topography, crystalline grain size, and surface roughness of the presented ZnO layers. The research of the crystalline grain size, as well as surface topography, over a relatively large surface area of $\sim 6 \times 6$ μm^2, was carried out by scanning electron microscopy (SEM; FEI Inspect S50, USA) with a magnification of x50000. The precise information about surface roughness (R_q — root mean square roughness) as a function of the deposition technology for the presented ZnO layer was obtained by an atomic force microscope (AFM; NTEGRA Prima, NT-MDT company, Russia). The ZnO surface was scanned in the semi-contact mode by a high-accuracy, high-resonance frequency (HA-HR) AFM probe (NT-MDT company, Russia), working with a resonance frequency equal to $f_r = 237.675$ kHz and scanning frequency of $f_s = 0.25$ Hz over a surface area of 5×5 μm^2. The next stage of the research was focused on the determination of the crystalline structure of the ZnO, ZnO/Pt, and ZnO/Pd layers. The investigation of the crystalline structure was carried out by means of Raman spectroscopy (NTEGRA Spectra, NT-MDT company, Russia). During these experiments, the ZnO layers were illuminated by a laser (LCM-S-111, Laser-export Co. Ltd., Russia) with a wavelength of $\lambda_c = 532$ nm. The chemical composition of the investigated ZnO layer was determined using the energy dispersive X-ray spectroscopy method

(EDS; QUANTAX XFlash, Bruker, USA), which was coupled with the SEM microscopy mentioned above. The structures of ZnO, ZnO/Pt, and ZnO/Pd were studied by the X-ray diffraction method (XRD), using the PANalytical Empyrean X-ray diffractometer, equipped with a Cu $K_{\alpha 1}$ radiation source and Johansson monochromator. Finally, the research focused on the investigation of sensing properties (changing of optical properties — spectral transmission) of ZnO, ZnO/Pt, and ZnO/Pd layers as a function of the structure's temperature over a range of T_s = 25–200°C or under the influence of a selected gaseous environment — hydrogen (carrier gas — synthetic air).

The experimental setup used for the aforementioned studies was composed of a measurement chamber with quartz windows and electric connections, a UV-VIS-NIR light source (Ocean Optics DT-Mini-2-GS), a spectrometer (Ocean Optics HR2000+), a temperature controller (Shimaden FP93), a temperature sensor (PT100), a ceramic heater, a PC computer, and a gas dispensing system. The investigated sample was placed into a measurement chamber, fixed by a holder, and connected to the ceramic heater. The temperature of the structure was measured by the PT100 sensor, which was in direct contact with the ZnO sensor layer. The gas dispensing system enables the preparation of gas mixtures delivered to the measurement chamber over a wide range of concentrations, namely from a few ppb (parts per billion) to several percent, depending on the used gas. Moreover, the system allows control of the gas mixture flow rate delivered to the measurement chamber from 5 to 500 cm^3/min. The scheme of the measurement setup and the gas dosing system are presented in Fig. 2a and 2b, respectively. The experimental results in a gaseous atmosphere were obtained for a 1–3% concentration of hydrogen (purity 99.999%, Linde Group), and in a carrier gas of synthetic air containing 20% O_2 and 80% N_2 (purity 99.999%, ALPHAGAZ™), the gas flow through the chamber was equal to f_g = 500 cm^3/min. The experiment was carried out in 30 min. cycles of poisoning and detoxification each, and the temperature of the tested ZnO layers stabilized at the level of T_s = 100°C.

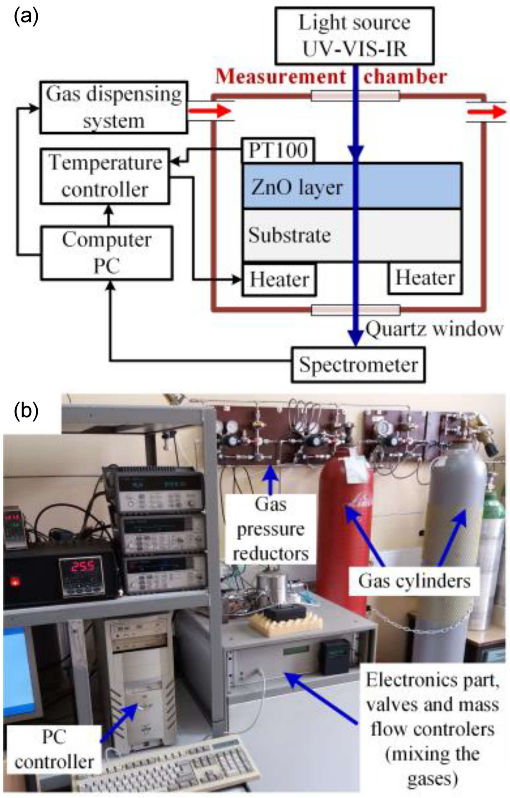

Fig. 2. Measurement setup; (a) scheme, (b) gas dispensing system.

4. Results

4.1. Surface topography of the ZnO layer

The ZnO surface topography, grain size, and surface roughness were initially investigated. The first investigated structure was a 550 nm-thick pure ZnO layer with relatively low roughness (continuous layer). The resulting SEM image is presented in Fig. 3a and shows that the surface of ZnO consists of small grains with a size of < 0.1 μm, and the layer is continuous with no observable cracks. In the case of porous ZnO, the layer consists of grains with free spaces between them (porous structure). The single grains size ranges are: porous ZnO — 0.06–0.4 μm (Fig. 3b), $\mathrm{ZnO/Pt_{DAO}}$ — 0.06–0.3 μm (Fig. 3c), $\mathrm{ZnO/Pt_{DBO}}$ — 0.07–0.4 μm (Fig. 3d), $\mathrm{ZnO/Pd_{DAO}}$ — 0.09–0.3 μm (Fig. 3e), and $\mathrm{ZnO/Pd_{DBO}}$ — 0.09–0.4 μm (Fig. 3f).

The detailed analysis of the surface structure, the investigation of the surface topography and surface roughness (root mean square roughness, R_q) as well as the 3D visualization of the ZnO layers were carried out using AFM. In the case of the pure ZnO layer, the R_q parameter is at the level of single nanometers (the AFM image of this layer is presented in Fig. 4a). In the case of the porous ZnO layer (Fig. 4b), the porous $\mathrm{ZnO/Pt_{DAO}}$ (Fig. 4c), and the $\mathrm{ZnO/Pd_{DAO}}$ (Fig. 4e) layer, the root mean square roughness is $R_q \sim 45$ nm. In the case of the porous $\mathrm{ZnO/Pt_{DBO}}$ (Fig. 4d) and the $\mathrm{ZnO/Pd_{DBO}}$ (Fig. 4e) layer, the root mean square roughness is $R_q \sim 60$ nm (Fig. 4f). It should be noted that the lower surface roughness, when compared to the $\mathrm{ZnO/Pt_{DBO}}$ or $\mathrm{ZnO/Pd_{DBO}}$ layer (where the Pt or Pd metallic layer was deposited before the oxidation process), occurs in the $\mathrm{ZnO/Pt_{DAO}}$ or $\mathrm{ZnO/Pt_{DAO}}$ structure (where the Pt or Pd layer was deposited after oxidation of the structure) and is $R_q \sim 45$ nm. This could be caused by the metallic layer, which

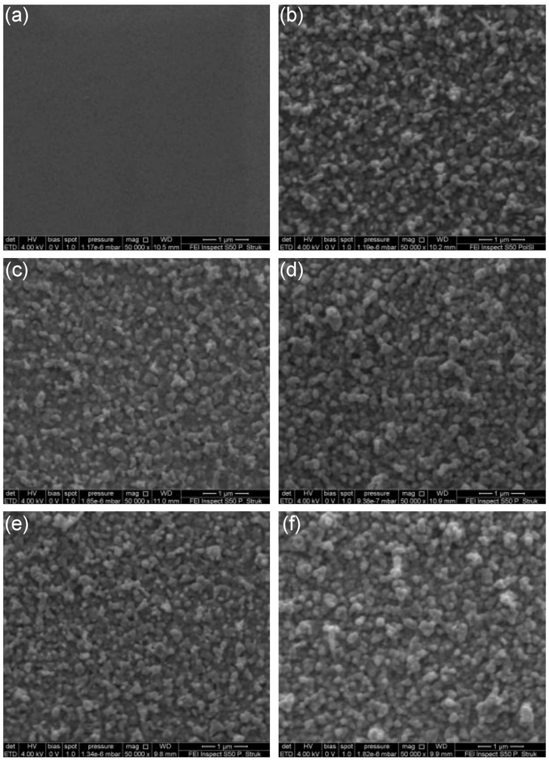

Fig. 3. Surface topography obtained by SEM method: (a) pure ZnO layer with low roughness; (b) porous ZnO layer; (c) porous ZnO/Pt$_{\mathrm{DAO}}$ layer; (d) porous ZnO/Pt$_{\mathrm{DBO}}$ layer; (e) porous ZnO/Pd$_{\mathrm{DAO}}$ layer; and (f) porous ZnO/Pd$_{\mathrm{DBO}}$ layer.

TABLE I

Root mean square roughness R_q of the investigated ZnO layer.

Sample	Root mean square roughness R_q [nm]
Pure ZnO	2.25
Pure, porous ZnO	40.4
Porous ZnO/Pt$_{\mathrm{DAO}}$	40.5
Porous ZnO/Pt$_{\mathrm{DBO}}$	57.7
Porous ZnO/Pd$_{\mathrm{DAO}}$	45
Porous ZnO/Pd$_{\mathrm{DBO}}$	66.0

DBO — Pt or Pd deposition before oxidation

DAO — Pt or Pd deposition after oxidation

was introduced and diffused into ZnO pores. The parametrized information on the surface roughness of the structures is presented in Table I.

4.2. Raman spectroscopy

The structural investigation of the presented ZnO layers was carried out using Raman spectroscopy. The ZnO semiconductor in the wurtzite-type of crystalline structure (bulk form) belongs to the space group C_{6v}^{4} in Schoenflies notation. In this case, all atoms occupy C_{3v} sites [20–25]. The group theory (in the Brillouin zone center) describes optical phonon modes as $\Gamma_{opt} = A_1 + 2B_1 + E_1 + 2E_2$ [26–31]. The phonons A_1, as well as E_1, are polar and split into longitudinal-optical (LO) and transverse-optical (TO) phonons with different frequencies [20–25]. The B1 modes are inactive in Raman scattering (silent modes) [24].

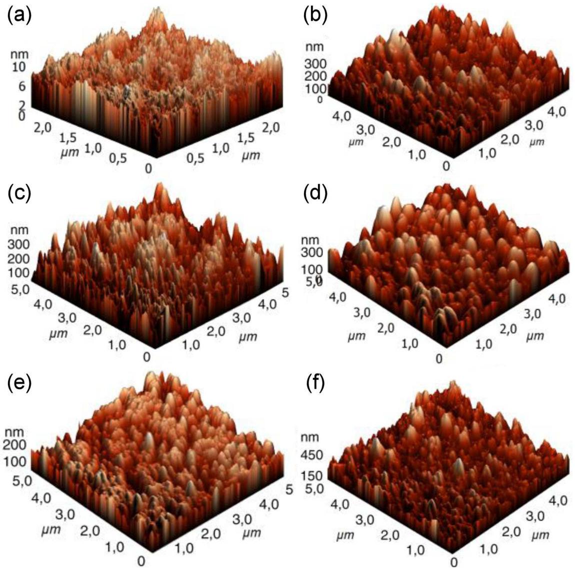

Fig. 4. Surface topography obtained by AFM: (a) pure ZnO layer with low roughness, (b) porous ZnO layer, (c) porous ZnO/Pt$_{\mathrm{DAO}}$ layer, (d) porous ZnO/Pt$_{\mathrm{DBO}}$ layer, (e) porous ZnO/Pd$_{\mathrm{DAO}}$ layer, and (f) porous ZnO/Pd$_{\mathrm{DBO}}$ layer.

The peak positions on the Raman spectra deliver information about the structure of the investigated ZnO layers. In accordance with the literature [22, 23], the following peaks for ZnO correspond to: 329 cm^{-1} — acoustic mode A_1, 380 cm^{-1} — acoustic mode A_1 (TO) phonon, 410 cm^{-1} — E_1 transverse optical phonon, 436 cm^{-1} — E_2, and 585 cm^{-1} — E_1 longitudinal optical phonon (LO). The measured Raman spectrum for the pure ZnO layer (low roughness) is presented in Fig. 5a and shows that a typical signature of a ZnO layer is in the form of the wurtzite crystalline structure. The presented Raman peaks are consistent with the literature data mentioned above, namely the peaks at 338 cm^{-1}, 382 cm^{-1}, and 410 cm^{-1} are hardly visible, and the peaks at 446 cm^{-1}, 491 cm^{-1}, and 588 cm^{-1} are more prominent. The small shift between the position of Raman peaks in the literature and the results presented above could be caused by the different crystalline size of the ZnO film [7]. The visible Raman peak close to 490 cm^{-1} is caused by the substrate (quartz — fused silica). The Raman spectrum for the porous (pure) ZnO layer is

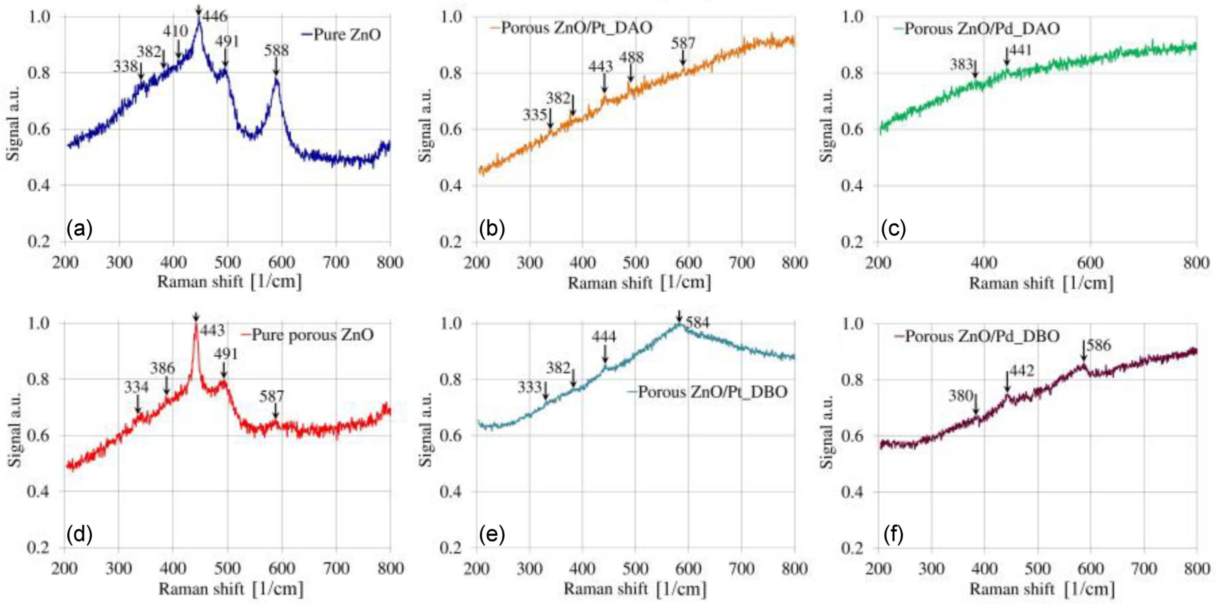

Fig. 5. The Raman spectra of ZnO layers: (a) pure ZnO layer with low roughness, (b) porous ZnO/Pt_{DAO} layer, (c) porous ZnO/Pd_{DAO} layer, (d) porous ZnO layer, (e) porous ZnO/Pt_{DBO}, and (f) porous ZnO/Pd_{DBO}.

presented in Fig. 5d, with clearly visible Raman shift peaks at 443 cm^{-1} and hardly visible peaks at 334 cm^{-1}, 386 cm^{-1}, and 587 cm^{-1}. The presented Raman spectra suggest that the pure ZnO layer is characterized by the wurtzite structure. The Raman spectra for the porous ZnO layer covered by a 5-nm-thick Pt layer or 5-nm-thick Pd layer (deposited after oxidation) are presented in Fig. 5b and 5c, respectively. In these Raman spectra, there are barely visible characteristic peaks for ZnO, which could be caused by a 5nm-thick metallic layer that blocks the Raman signal from the sample or the structure of the ZnO film could be partially amorphous. The Raman spectra for the ZnO layer covered by a 5-nm-thick Pt layer or 5-nm-thick Pd layer, deposited before the annealing and oxidizing process, are presented in Fig. 5e and 5f, respectively. The peaks in Raman spectra for the ZnO/Pt_{DBO} layer are hardly visible for 333 cm^{-1}, 382 cm^{-1}, 444 cm^{-1}, and 584 cm^{-1}. For the ZnO/Pd_{DBO} layer, the resulting Raman spectra peaks at 380 cm^{-1}, 442 cm^{-1}, and 586 cm^{-1} are hardly visible.

TABLE II

Analysis of the chemical composition of the investigated ZnO layer.

	Element [at.%]			
	Zn	O	Pt	Pd
Pure ZnO	48.95	51.05	0	0
Pure, porous ZnO	43.84	56.19	0	0
Porous ZnO/Pt_{DAO}	45.72	52.24	2.06	0
Porous ZnO/Pt_{DBO}	45.69	52.17	2.15	0
Porous ZnO/Pd_{DAO}	47.59	50.15	0	2.26
Porous ZnO/Pd_{DBO}	46.89	50.67	0	2.44

4.3. Energy-dispersive X-ray spectroscopy (EDS)

The chemical composition of the presented ZnO layers was measured by energy-dispersive X-ray spectroscopy (EDS using a QUANTAX, XFlash 6, Bruker). The obtained EDS spectra of the investigated pure and porous ZnO layers confirmed that the layers consist of zinc and oxygen, as clearly visible peaks from the respective elements are presented in Fig. 6a and 6d (the silicon is attributed to the quartz substrate). For the Pt-doped ZnO layer, the EDS shows peaks from Zn and O, as well as the expected Pt peak (see Fig. 6b and 6e). Likewise, for the Pd-doped ZnO layer, besides the peaks from Zn and O elements, the Pd peak is clearly visible in the EDS spectra presented in Fig. 6c and 6f.

Detailed information on the chemical composition of each investigated ZnO layer is presented in Table II. It should be noted that the EDS method confirms that the tested ZnO, ZnO/Pt, and ZnO/Pd layers have a high chemical purity and do not contain any impurities from other elements.

4.4. X-ray diffraction

XRD $2\Theta/\Theta$ scans collected for the samples are shown in Fig. 7. All the samples exhibit strong lines related to diffraction from the (10.0), (00.2),

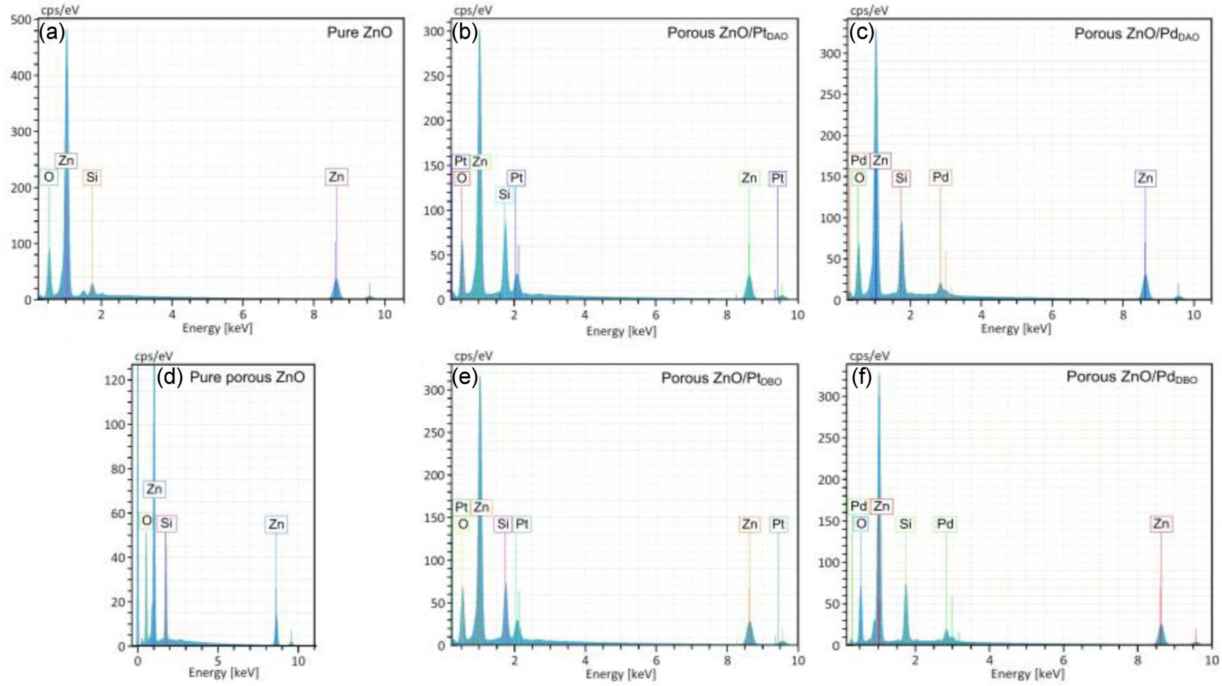

Fig. 6. Chemical composition of ZnO layer measured by EDS methods: (a) pure ZnO layer with low roughness, (b) porous ZnO/Pt_{DAO} layer, (c) porous ZnO/Pd_{DAO} layer, (d) porous ZnO layer, (e) porous ZnO/Pt_{DBO}, and (f) porous ZnO/Pd_{DBO}.

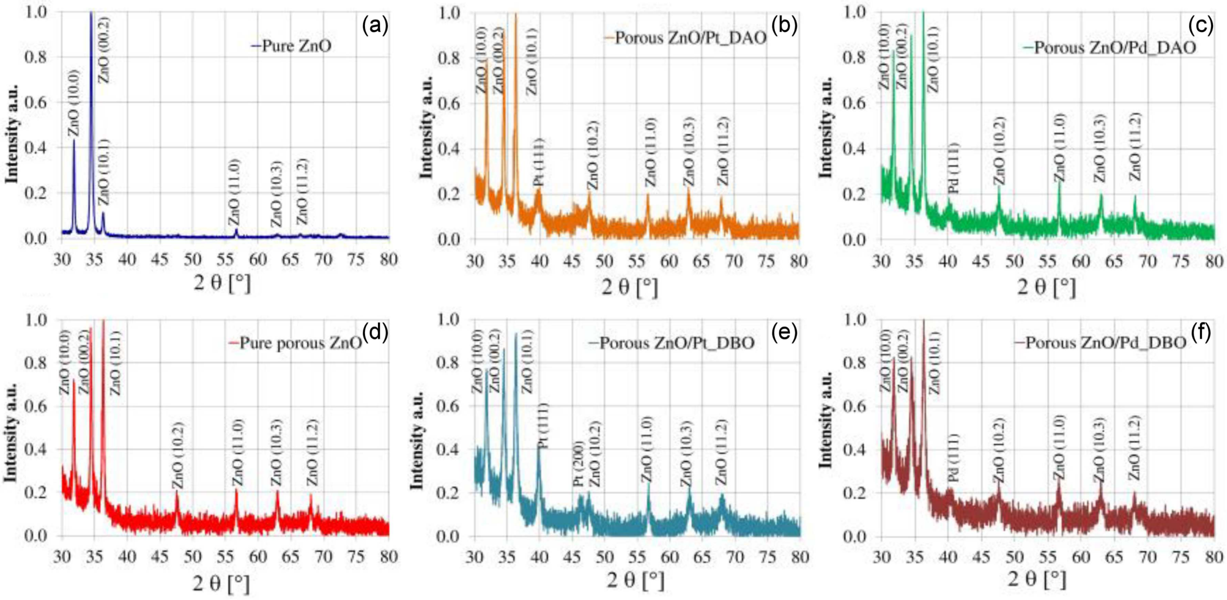

Fig. 7. X-ray diffraction patterns of ZnO layers: (a) pure ZnO layer with low roughness, (b) porous ZnO/Pt_{DAO} layer, (c) porous ZnO/Pd_{DAO} layer, (d) porous ZnO layer, (e) porous ZnO/Pt_{DBO}, and (f) porous ZnO/Pd_{DBO}.

and (10.1) planes in the range of 30–37°. For the non-porous ZnO, these lines dominate the whole patterns, whereas for the porous samples, their intensity is lower, and additional ZnO lines are visible from the ZnO planes (10.2), (11.0), (10.3), and (11.2). The samples with platinum and palladium differ by the presence of the peaks originating from diffraction from Pt (111) and Pd (111) around 40° for both metals, due to their similar unit cell. In the case of Pt, also the (200) line is visible around 47° for the Pt_{DBO} sample, which is related to the higher intensity of the (111) line for that sample,

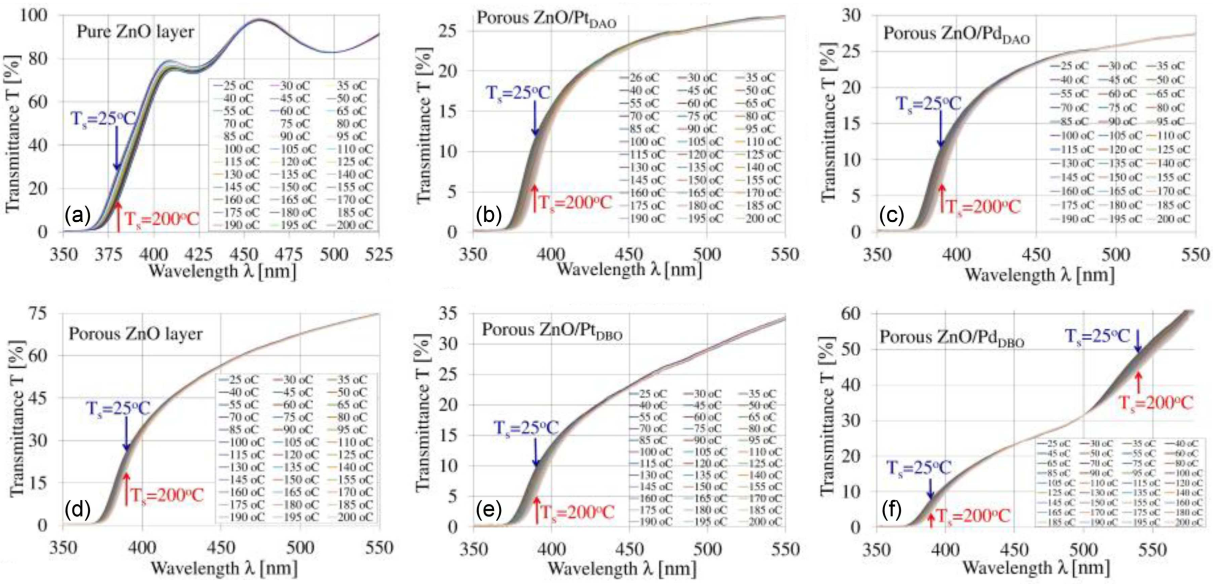

Fig. 8. Optical properties of ZnO layer — spectral transmittance: (a) pure ZnO layer with low roughness, (b) porous ZnO/Pt$_{DAO}$ layer, (c) porous ZnO/Pd$_{DAO}$ layer, (d) porous ZnO layer, (e) porous ZnO/Pt$_{DBO}$ layer, and (f) porous ZnO/Pd$_{DBO}$ layer.

which can be interpreted as the result of the formation of larger Pt grains than in the case of Pt$_{DAO}$. For palladium, no such difference could be observed, and Pd$_{DAO}$ and Pd$_{DBO}$ show almost identical patterns. The mean crystallite sizes in a direction perpendicular to the surface were calculated from the Scherrer equation for selected peaks. The crystallite sizes extracted from the ZnO (10.0) XRD line for porous ZnO (35.08 nm) are almost the same as those obtained for Pt-doped porous ZnO (34.05 nm) and larger than the ones seen for Pd-doped porous ZnO (25.86 nm), showing that the addition of Pd influences the transformation of Zn to ZnO yielding smaller mean crystallite sizes.

4.5. Optical properties of ZnO layers — sensor applications

The optical properties of the ZnO wide band gap oxide semiconductor depend on the fabrication technology and deposition parameters, doping materials, and the wavelength of the light utilized during experimentation. Among the optical properties of the semiconductor materials, the significant parameters are the spectral transmission and absorption edge, which are dependent on the energy band gap. The absorption edge for the presented ZnO layer is at $\lambda_a \sim 370$ nm; above the absorption edge, the ZnO layer is transparent to light. The highest optical transmission is at $T \sim 90\%$ for the pure ZnO layer (low roughness) (see Fig. 8a). The porous ZnO layer without doping is characterized by spectral transmission at the level of $T \sim 70$–90% in the VIS-NIR spectrum (see Fig. 8d). The doping of the ZnO layer with palladium or platinum causes a decrease in the spectral transmission of light through the layer. The spectral transmission for the porous ZnO layer doped with Pt or Pd is at a level of $T \sim 25$–30% in the VIS region, as shown in Fig. 8b and 8c, respectively. The oxidation and annealing process increases the spectral transmission in the ZnO/Pt layer up to 35% in the VIS range (see Fig. 8e). A significant increase in the spectral transmission of light from $T \sim 27\%$ to $T \sim 75\%$ in the VIS range is observed for the ZnO/Pd layer after the oxidation and annealing process (see Fig. 8f). The higher spectral transmission of ZnO/PdDBO in comparison to other ZnO/Pt or ZnO/Pd layer of could be caused by better oxidation of ZnO layer and partial oxidation of Pt and Pd during thermal technological process.

4.5.1. Structure of ZnO temperature sensors

The principle of operation of a semiconductor temperature sensor is based on changing the energy band gap as a function of temperature. The energy band gap as a function of temperature could be described by the Varshni relation [32]

$$E_g\left(T_t\right) = E_g\left(0\right) + \frac{r\,T_t^2}{\left(T_t+\beta\right)}, \tag{1}$$

where T_t is temperature, $E_g(T), E_g(0)$ — the energy band gap for temperature $T = 0$ K, r and β — the fitting parameter characteristics for the semiconductor material.

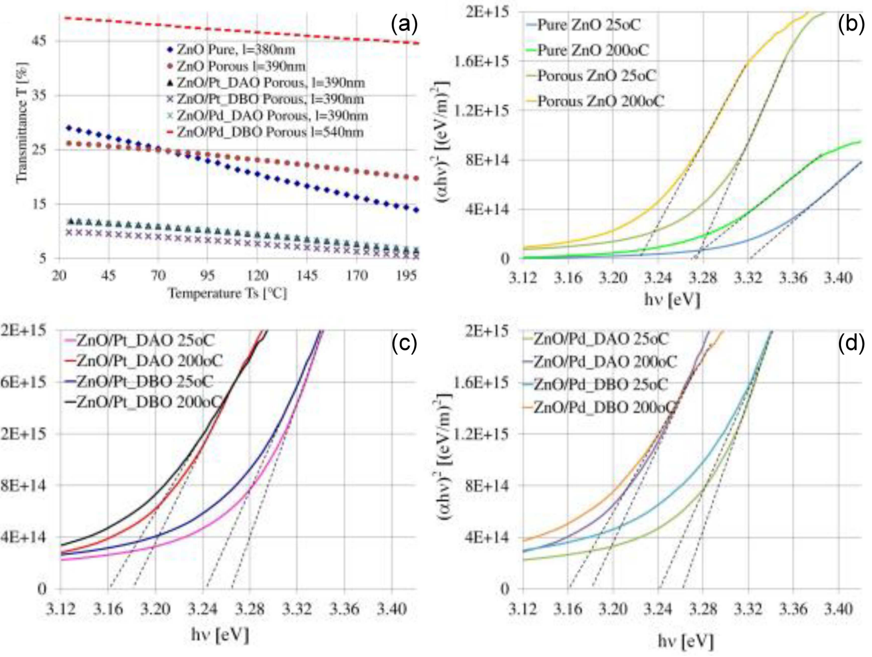

Fig. 9. Transmission of light for a selected wavelength through ZnO layers as a function of temperature (a). Plots of the function of $(\alpha h\nu)^2 = f(h\nu)$ for: (b) pure and porous ZnO layers at 25°C and 200°C, (c) ZnO/Pt layers, (d) ZnO/Pd layers.

The energy band gap for a direct band semiconductor can be calculated based on a spectral transmission of light and the analysis of the absorption coefficient α [26, 33, 34]

$$I = I_0\,\mathrm{e}^{-\propto d}, \tag{2}$$

$$\propto = -\frac{\ln(\mathrm{T})}{d}, \tag{3}$$

$$(\propto h\nu)^2 = C\,(h\nu - E_g), \tag{4}$$

where $\mathrm{T} = I/I_0$ is the transmittance of light, d — layer thickness, C — a constant depending on the electron–hole mobility, h — the Planck constant, ν — the frequency of light.

In the range close to the absorption edge, the $(\propto h\nu)^2$ versus photon energy $(h\nu)$ is a nearly linear function. The energy band gap could be determined by extrapolation of the linear region of the function (4). It should be noted that the pure ZnO layers are solid and homogeneous with thickness d. In a presented analysis for the ZnO porous layers, the approximation was made that the thickness of the porous layer corresponds to the geometric thickness d.

The determination of the spectral transmission changes as a function of an external condition, namely the temperature (T_s = 25–200°C) of the ZnO structure, was completed next. The increase in temperature induces changes in the transmission corresponding to a shift of the absorption edge (initially around 380 nm) to longer wavelengths in most of the presented pure and porous ZnO, ZnO/Pt, and ZnO/Pd layers. Such narrowing of the energy gap with increasing temperature was reported in the literature for ZnO and other metal oxides [35] and is caused by thermal expansion of the crystal lattice. However, for the ZnO/Pd layer, where the Pd was deposited before the oxidation and annealing process, the maximum temperature sensitivity shifted from the UV range (~ 390 nm) to VIS range (~ 540 nm) (Fig. 8f). The shift of the maximum temperature sensitivity from the UV to VIS range could be due to doping of ZnO with Pd, as well as the oxidation and annealing process, and creation of ZnO–Pd conglomerates in the layer. The ZnO–Pt conglomerates could cause changes in the energy band gap or changes in the Fermi level in the semiconductor. The modulation of the Fermi level of the ZnO semiconductor doped with the catalytic material has also been reported by Drmosh [28]. This suggests that in the presented structure, the photon with a lower energy of ~ 2.2 eV (in comparison to 3.2 eV for other ZnO structures) could also be absorbed.

The observed phenomenon can be utilized in ZnO/Pd layer temperature sensors, which can operate in the visible range of light. The temperature sensitivity in the visible region of light is an important advantage of the presented ZnO/Pd$_{\mathrm{DBO}}$ structure in comparison to other works [26, 33, 34], where the authors presented changes in optical parameters (spectral transmission) of ZnO as a function of temperature, which occurred only in the UV range.

Operation of the temperature sensor in the visible range of light is a desirable feature from the point of view of the component cost (sources and light

The energy band gap and temperature sensitivity of the ZnO layer. TABLE III

Parameter	Pure ZnO	Pure, porous ZnO	Porous ZnO/Pt_{DAO}	Porous ZnO/Pt_{DBO}	Porous ZnO/Pd_{DAO}	Porous ZnO/Pd_{DBO}
Temperature T_s [°C]	Energy band gap E_g [eV]					
25	3.32	3.27	3.26	3.24	3.26	3.24
200	3.27	3.22	3.18	3.16	3.18	3.16
Optical properties						
Wavelength λ [nm]	380	390	390	390	390	390/540
Temperature sensitivity$_{\max}$ [%/°C]	−0.088	−0.037	−0.031	−0.026	−0.030	−0.020/−0.027

detectors on the VIS range) and the final cost of the application-ready sensor structure. The parameterization of this changing transmission of light over a selected wavelength as a function of temperature is presented in the form of a graph (see Fig. 8a–e and Fig. 9a). The temperature sensitivity of the investigated ZnO layers is presented in Table III. The highest temperature sensitivity occurs for the pure ZnO layer. For the porous ZnO layer, the highest temperature sensitivity is for the pure layer. Doping the ZnO layer with Pt or Pd decreases the temperature sensitivity, especially in the case where the Pd and Pt layers were deposited before any oxidation and annealing processes.

The presented experimental results showed that the deposition technology (described in detail in Sect. 2), structure, and chemical composition of ZnO, ZnO/Pt, and ZnO/Pd layers have an impact on the width of the energy band gap. The highest energy band gap is observed for the smooth ZnO layer, namely $E_g = 3.32$ eV (deposition: target ZnO, O_2/Ar atmosphere). The porous ZnO layer (deposition: target Zn, O_2/Ar atmosphere, oxidation, and annealing process) is characterized by a lower energy band gap, namely $E_g = 3.27$ eV (Fig. 9b). The deposition of a Pt or Pd (5 nm) layer on porous ZnO after an oxidation and annealing process does not affect the energy band gap ($E_g = 3.26$ eV). However, if Pt or Pd layers were deposited on porous ZnO before the oxidation and annealing process, the energy band gap was decreased to $E_g = 3.24$ eV (Fig. 9c and d). It could be due to the impediment of the oxidation process through the thin metal layer of ZnO. The energy band gap of ZnO layers for the temperature of 25°C as well as of 200°C is presented in Table III.

4.5.2. Structure of ZnO gas sensors

The ZnO layer also has possible applications as an active part of gas sensor structures for the detection of selected gas environments. Below, the preliminary experimental results are presented, focused on the research of sensing properties — changes in spectral transmission of light as a function of the selected gas environment, i.e., hydrogen H_2. The research was carried out for a porous ZnO layer doped by platinum or palladium deposited before or after the annealing and oxidation process.

The sensing mechanism of reducing gas — hydrogen — by an n-type semiconductor (ZnO) is based on the adsorption, desorption, and chemisorption of atoms on the semiconductor surface. The molecular hydrogen is dissociated into atomic hydrogen (which is highly reactive in contact with the semiconductor surface) by a catalytic material, i.e., palladium or platinum [28–31]. The oxygen from the environment is adsorbed on the semiconductor surface, and the created oxygen ions cause the electrons to be extracted from the conductivity band and increase the resistance of the structure (and hence decrease conductivity). The poisoning of the semiconductor structure by hydrogen causes the reaction of adsorbed hydrogen ions with oxygen ions. As a result of the reaction, the electrons are returned to the conduction band, and hence, the resistance of the semiconductor structure is decreased (conductivity increases) [28–31]. It should be noted that the electrical properties of semiconductor materials are directly connected with optical properties, such as transmission and absorption edge. The changes in electrical properties of the semiconductor (ZnO) cause simultaneous changes in optical properties, which could be used as a basis for the operation of optoelectronic gas sensors. It should be noted that the structure of the ZnO layer (surface roughness) and the crystalline grain size have an impact on the sensitivity properties of the ZnO layer. According to our previous study, presented by Struk et al. in [10], the ZnO layer with a smooth surface is not sensitive to the external gaseous environment of hydrogen. Whereas the pure porous ZnO structure, which is characterized by a highly developed structure (in the form of nanograins), is sensitive to changes in the gas environment, including hydrogen. In the presented ZnO/Pt layers, changes in optical properties under the influence of 1–3% hydrogen (a lower explosion limit for hydrogen is 4 mol%) in the atmosphere of synthetic air were at a low level. Only for the ZnO/Pt_{DAO} structure, where the Pt layer was deposited after the annealing and oxidation process, there are visible small changes in spectral transmission, but only for the first three cycles of poisoning and detoxification;

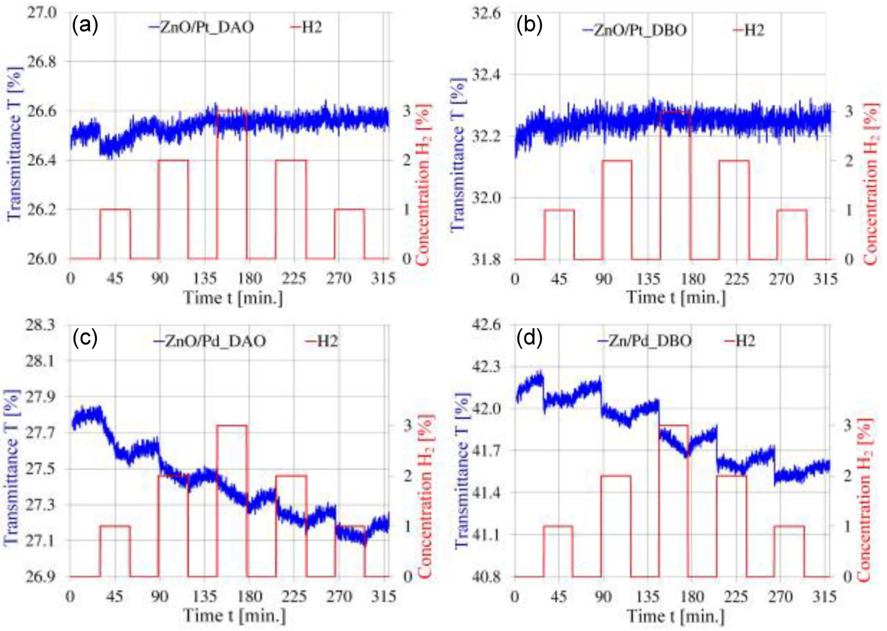

Fig. 10. Changes in the optical transmission for λ = 540 nm of the porous ZnO layer exposed to H_2: (a) ZnO/Pt_{DAO}, (b) ZnO/Pt_{DBO}, (c) ZnO/Pd_{DAO}, and (d) ZnO/Pd_{DBO}.

for the remaining cycles the presented layer was probably saturated and insensitive to changes of the gas (see Fig. 10a). In the case of the nO/Pt_{DBO} structure, where the Pt layer was deposited before the annealing and oxidation process, the changes in spectral transmission under the influence of 1–3% hydrogen in the atmosphere of synthetic air are practically invisible, which means that the structure was insensitive to hydrogen (see Fig. 10b). It could be caused by a too high level of Pt doping.

For the ZnO/Pd layers, the changes in the transmission of light under the influence of a 1–3% hydrogen atmosphere are clearly visible in Fig. 10c and 10d. Particularly in the case of the ZnO/PdDBO sample, where the Pd layer was deposited before the annealing and oxidation processes, the sensitivity under the influence of hydrogen atmosphere is greater than that for ZnO/Pd_{DAO}, where the Pd layer was deposited after the annealing and oxidation processes. The annealing process could cause the palladium, which is a catalytic layer, to penetrate deeper into the porous ZnO and hence increase the active surface, which is in contact with the hydrogen gas and thus increases the transmission changes under the influence of hydrogen.

5. Conclusions

The physical properties of the ZnO layer are directly related to the deposition technology and the type of doping elements of the layers. The ZnO layer deposited by reactive magnetron sputtering can form a continuous layer (smooth layer with a surface roughness of $R_q = 2.3$ nm), or the layer can have a porous structure with a highly developed surface ($R_q \sim 40$–66 nm). It should also be noted that the presented ZnO layers have high purity without any contamination, which is confirmed by EDS. The presented experimental results show that the ZnO semiconductor material can be applied as an active sensor part for the detection of a hydrogen gaseous environment (ZnO/Pd) and as a temperature sensor. As for the temperature sensor, it functions in the UV range (pure, porous, ZnO/Pt, ZnO/Pd) and in the visible light region (ZnO/Pd_{DBO} structure). In summary, the results are a basis for the development of optoelectronic sensors, which serve the purpose of detecting hydrogen or temperature measurement.

Acknowledgments

The research was sponsored by the grant WND-POIG.01.03.01-00-159/08-00 InTechFun.

References

[1] P. Kokayeff, S. Zink, P. Roxas, in: *Handbook of Petroleum Processing*, Eds. S.A. Treese, D.S. Jones, P.R. Pujado, Springer, 2020 p. 1.

[2] Y. Haseli, *Int. J. Hydrogen Energy* **43**, 9015 (2018).

[3] R. Ramachandran, R. Menon, *Int. J. Hydrogen Energy* **23**, 593 (1998).

[4] M.A. Borysiewicz, *Crystals* **9**, 505 (2019).

[5] Y. Wang, Y. Wang, X. Sun, M. Li, M. Tang, J. Cao, C. Qin, *Int. J. Hydrogen Energy* **50**, 1470 (2024).

[6] I. Cheng, C. Lin, F. Pan, *Appl. Surf. Sci.* **541**, 148551 (2021).

[7] M.A. Franco, P.P. Conti, R.S. Andre, D.S. Correa, *Sens. Actuators Rep.* **4**, 100100 (2022).

[8] V. Schröder, B. Emonts, H. Janßen, H.-P. Schulze, *Chem. Eng. Technol.* **27**, 847 (2004).

[9] R. Jaaniso, O.K. Tan, *Semiconductor Gas Sensors*, 1st ed., Elsevier, 2013.

[10] P. Struk, T. Pustelny, K. Gołaszewska, M.A. Borysiewicz, A. Piotrowska, *Bull. Pol. Acad. Sci.* **63**, 829 (2015).

[11] C. Jagadish, S. Pearton, *Zinc Oxide Bulk, Thin Films and Nanostructures, Processing, Properties, and Applications*, 1st ed., Elsevier, Berlin 2006.

[12] S.K. Shaikh, V.V. Ganbavale, S.V. Mohite, U.M. Patil, K.Y. Rajpure, *Superlattices Microstruct.* **120**, 170 (2018).

[13] G. Eranna, *Metal Oxide Nanostructures as Gas Sensing Devices*, CRC Press, 2011.

[14] P. Listewnik, M. Hirsch, P. Struk, M. Weber, M. Bechelany, M. Jędrzejewska-Szczerska, *Nanomaterials* **9**, 306 (2019).

[15] P. Struk, T. Pustelny, K. Gołaszewska, E. Kamińska, M.A., Borysiewicz, M. Ekielski, A. Piotrowska, *Opto-Electron. Rev.* **21**, 376 (2013).

[16] H. Morkoç, U. Özgür, *Zinc Oxide: Fundamentals, Materials and Device Technology*, Wiley, 2009.

[17] S. Kumar, S.D. Lawaniya, S. Agarwal, Y.-T. Yu, S.R. Nelamarri, M. Kumar, Y.M. Mishra, K. Awasthi, *Sens. Actuators B Chem.* **375**, 132943 (2023).

[18] Y. Kang, F. Yu, L. Zhang, W. Wang, L. Chen, Y. Li, *Solid State Ion.* **360**, 115544 (2021).

[19] M.A. Borysiewicz, E. Dynowska, V. Kolkovsky, J. Dyczewski, M. Wielgus, E. Kamińska, A. Piotrowska, *Phys. Status Solidi (a)* **209**, 2463 (2012).

[20] C.F. Klingshirn, B.K. Meyer, A. Waag, A. Hoffmann, J. Geurts, *Zinc Oxide: From Fundamental Properties Towards Novel Applications*, Springer, 2010.

[21] R. Joswik, A.A. Dalinkevich, *Chemistry and Chemical Biology: Methodologies and Applications*, 1st ed., Apple Academic Press, 2014.

[22] R. Cuscó, E. Alarcón-Lladó, J. Ibáñez, L. Artús, J. Jiménez, B. Wang, M.J. Callahan, *Phys. Rev. B* **75**, 165202 (2007).

[23] A.K. Ojha, M. Srivastava, S. Kumar, R. Hassanein, J. Singh, M.K. Singh, A.A. Materny, *Vib. Spectrosc.* **72**, 90 (2014).

[24] B. Hadžić, N. Romčević, J. Trajić, R. Kostić, G. Stanišić, D. Timotijević, in: *Proc. of the III Advanced Ceramics and Applications Conf.* Eds. W. Lee, R. Gadow, V. Mitic, N. Obradovic, Atlantis Press, Paris 2016.

[25] S. Guo, Z. Du, S. Dai, *Phys. Status Solidi (b)* **246**, 2329 (2009).

[26] P. Cai, D. Zhen, X. Xu, Y. Liu, N. Chen, G. Wei, C. Sui, *Mater. Sci. Eng. B* **171**, 116 (2010).

[27] M. Wang, E.J. Kim, J.S. Chung, E.W. Shin, S.H., Hahn, K.E. Lee, C. Park, *Phys. Status Solidi (a)* **203**, 2418 (2006).

[28] Q.A. Drmosh, Z.H. Yamani, *Ceram. Int.* **42**, 12378 (2016).

[29] A.-T.T. Do, H.T. Giang, T.T. Do, N.Q. Pham, G.T. Ho, *Beilstein J. Nanotechnol.* **5**, 1261 (2014).

[30] A. Janotti, C.G. Van de Walle, *Rep. Prog. Phys.* **72**, 126501 (2009).

[31] N.H. Al-Hardan, M.J. Abdullah, A.A. Aziz, *Int. J. Hydrogen Energy* **35(9)**, 4428 (2010).

[32] Y.P. Varshni, *Physica* **34**, 149 (1967).

[33] K.J. Hong, T.S. Jeong, *J. Cryst. Growth* **280**, 545 (2005).

[34] C. Sui, J. Xia, H. Wang, T. Xu, B. Yan, Y. Liu, *Rev. Sci. Instrum.* **82**, 084901 (2011).

[35] Y. Cho, A. Yamaguchi, R. Uehara, S. Yasuhara, T. Hoshina, M. Miyauchi, *J. Chem. Phys.* **152(23)**, 231101 (2020).